analytical chemistry

pubs.acs.org/ac Article

Single-Cell and Subcellular Analysis Using Ultrahigh Resolution 21 T MALDI FTICR Mass Spectrometry

Daniel C. Castro, Karl W. Smith, Miles D. Norsworthy, Stanislav S. Rubakhin, Chad R. Weisbrod, Christopher L. Hendrickson, and Jonathan V. Sweedler*

Cite This: https://doi.org/10.1021/acs.analchem.3c00393 Read Online

ACCESS | Metrics & More | Article Recommendations | Supporting Information

ABSTRACT: The mammalian brain contains ~20,000 distinct lipid species that contribute to its structural organization and function. The lipid profiles of cells change in response to a variety of cellular signals and environmental conditions that result in modulation of cell function through alteration of phenotype. The limited sample material combined with the vast chemical diversity of lipids makes comprehensive lipid profiling of individual cells challenging. Here, we leverage the resolving power of a 21 T Fourier-transform ion cyclotron resonance (FTICR) mass spectrometer for chemical characterization of individual hippocampal cells at ultrahigh mass resolution. The accuracy of the acquired data allowed differentiation of freshly isolated and cultured hippocampal cell populations, as well as finding differences in lipids between the soma and neuronal processes of the same cell. Differences in lipids include TG 42:2 observed solely in the cell bodies and SM 34:1;O2 found only in the cellular processes. The work represents the first mammalian single cells analyzed at ultrahigh resolution and is an advance in the performance of mass spectrometry (MS) for single-cell research.

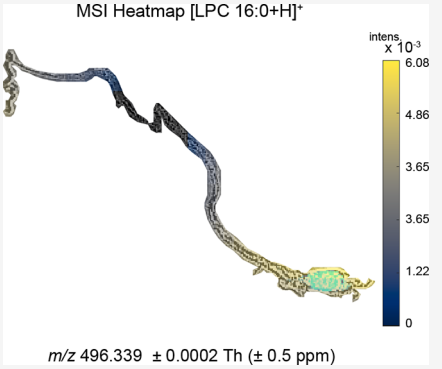

INTRODUCTION

Lipids represent one of the most chemically complex families of cellular molecules. Lipid profiles are often cell type and cell state specific with some of the highest complexities known to be found in neuronal cells. Cellular lipids have a variety of origins including dietary intake and biosynthesis.[1,2] Lipid profiles can change upon a variety of intracellular and extracellular signals, as well as during alteration of extracellular environments. For example, placing cells in culture can influence both enzymatic and nonenzymatic reactions that alter membrane lipid composition leading to changes in membrane fluidity and inter- and intracellular signaling.[3,4] Often developing in culture, oxidative stress activates biological pathways not typically seen in in vivo and leads to the synthesis of diverse bioactive lipids that exhibit either beneficial or detrimental effects on cell survival and/or function.[5,6] The brain contains ~20,000 distinct lipid species (different head groups, tails, chain lengths, substitutions, and many positional isomers), and the lipid profiles of these cells demonstrate different levels of heterogeneity even in cases of cells of the same cell type.[7] Therefore, comprehensive characterization of cellular lipid profile heterogeneity is critical for the understanding of cellular structural organization and function in both physiological and pathological states.[8−11]

The untargeted and simultaneous detection of multiple lipid classes has made mass spectrometry (MS) a prevailing technique for characterizing lipids in biological samples, leading to the emergence of the field, "lipidomics". Traditionally, lipidomic experiments were performed using MS on lipid extracts obtained from bulk-tissue samples, thereby only providing a global view of lipid changes.[12,13] Recent enhancements in MS approaches allow lipid characterization in thousands of isolated individual cells.[14] The small diameter of the laser probe footprint achievable in matrix-assisted laser desorption/ionization (MALDI) MS makes direct measurements of relatively dense cellular populations that were deposited on a glass slide surface possible. Moreover, multiple acquisitions at different locations of the same cell can be performed revealing both intracellular and intercellular chemical heterogeneity.[15−17] Unfortunately, identification of detected analytes using tandem-MS, a typical approach for structural characterization, is hampered by the limited sample material present in a single-cell or subcellular structure. To address this challenge, an approach can be used in which experimentally measured analyte masses of interest found in single-cell measurements are matched to published information and data obtained using similar "omic" approaches (e.g., liquid chromatography tandem-MS-based lipidomics). Therefore, accurate measurement of monoisotopic molecular mass is

Received: January 26, 2023
Accepted: April 4, 2023

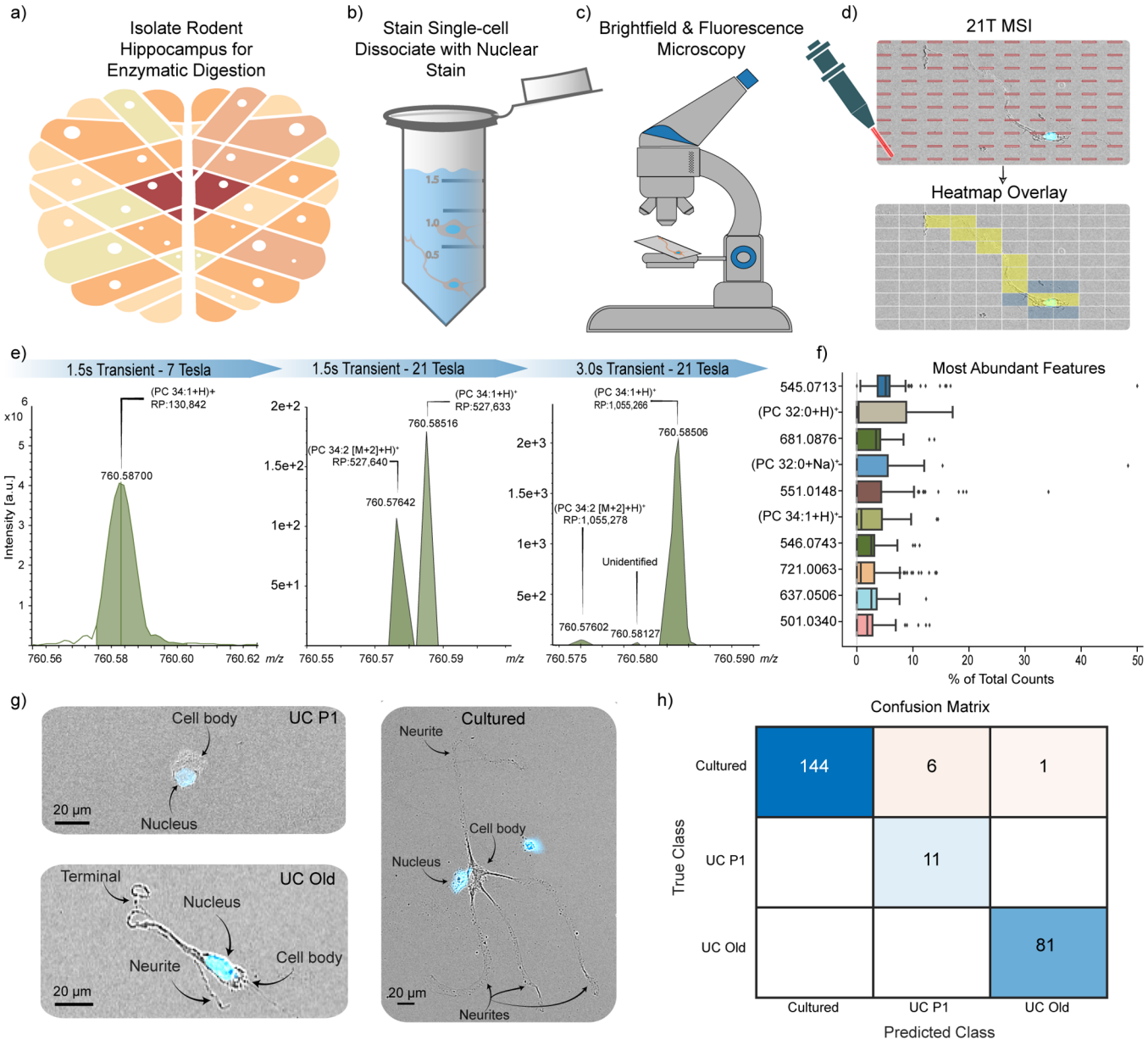

Figure 1. Single-cell mass spectrometry imaging (MSI) workflow using a 21 T FTICR MS. (a–d) Schematic of single-cell MSI acquisition and data analysis. (e) Differentiation of three isobaric peaks at $m/z \sim 760$ with the 21 T FTICR mass spectrometer. Using a similar transient acquisition time on a 7 T FTICR mass spectrometer shows only one prominent peak when compared to the 21 T. Increasing the transient acquisition time from 1.5 to 3.1 s on the 21 T FTICR mass spectrometer increased the resolving power at m/z 760.58506 from 527,633 to 1,055,266 allowing the differentiation of (PC 34:1 + H)$^+$ and m/z 760.58127 from (PC 34:2 [M + 2] + H)$^+$, where (PC 34:2 [M + 2] + H)$^+$ represents the n + 2 isotope of (PC 34:2 + H)$^+$. (f) Most abundant mass spectral features in single-cell 21 T FTICR MS analysis. The most abundant mass spectral features were determined by calculating the m/z feature that had the highest intensity value in each cell, across all the cells. Putatively identified features include m/z 734.5686 (PC 32:0 + H)$^+$ and its sodiated adduct at m/z 756.5518 (PC 32:0 + Na)$^+$, as well as m/z 760.5851 (PC 34:1 + H)$^+$. (g) Merged brightfield and fluorescent microscopy images of UC P1, Cultured (4 days), and UC Old cells. UC P1 and Cultured cells ranged in length from ~15 to 30 and ~150 to 400 μm, respectively. The smaller lengths indicate that only the cell body was isolated. Larger values indicate the presence of cell terminals typically outgrown during cell culture. (h) Confusion matrix using the top 100 m/z features for the classification between the groups.

critical for analyte identification in single-cell and subcellular MS analysis, where the best results can be obtained with ultrahigh resolution mass spectrometers, such as Fourier-transform ion cyclotron resonance (FTICR) mass spectrometers. FTICR MS currently offers the highest mass accuracy and mass resolution, providing parts-per-billion (ppb) mass errors with over 1,000,000 resolving power routinely.[18] Increased magnetic field strength raises resolving power linearly and increases mass accuracy quadratically without requiring longer transient acquisition times.[19] Longer transient acquisition times not only add substantial measurement overhead but can also be unrealistic in single-cell measurements due to the limited amount of sample material where rapid signal loss can occur due to the collision of analyte ions with residual background gas.[20] The increase in mass resolution results in greater analyte coverage due to the

https://doi.org/10.1021/acs.analchem.3c00393
Anal. Chem. XXXX, XXX, XXX−XXX

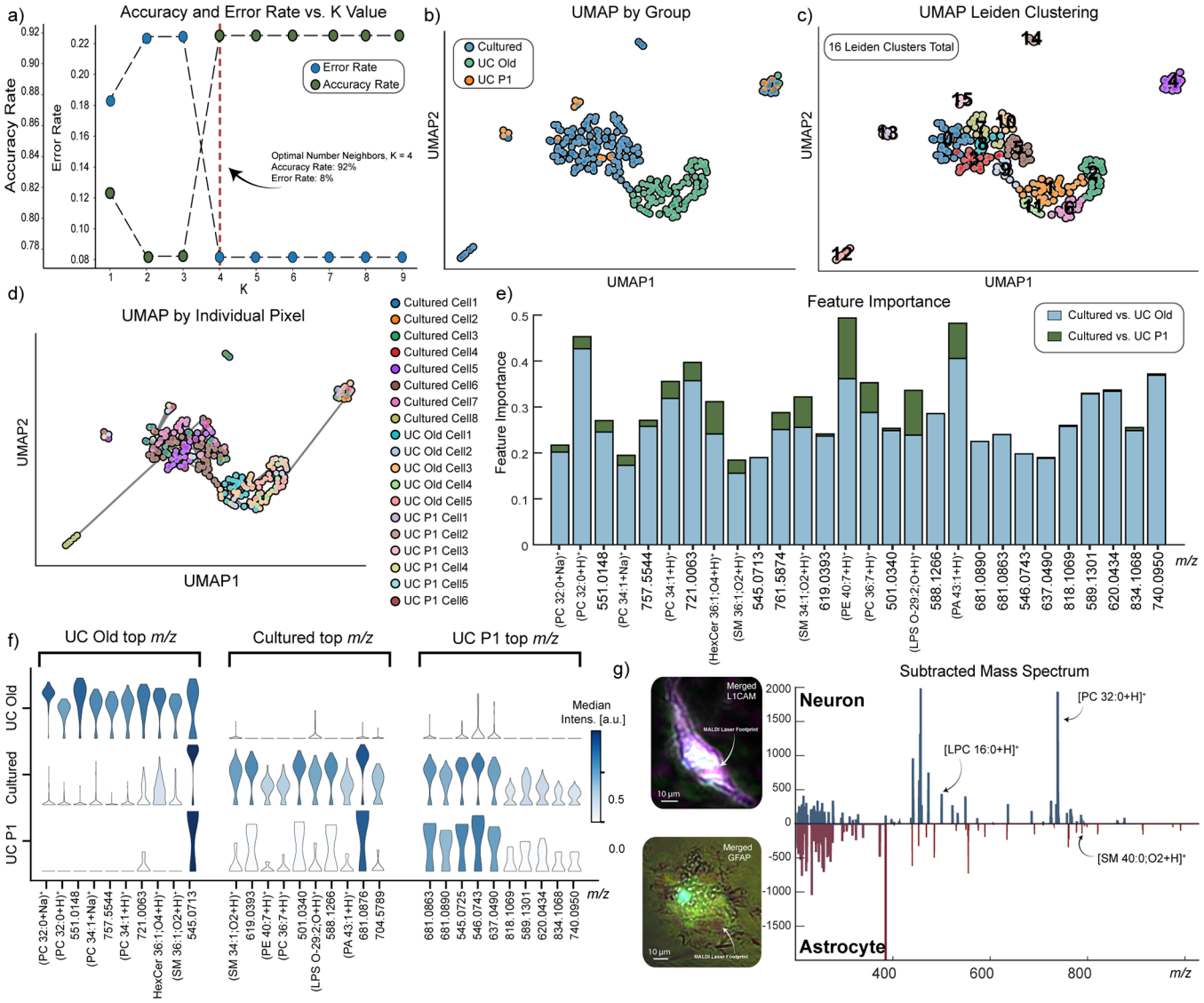

Figure 2. Single-cell 21 T FTICR MS data analysis: UMAP embedding, cell classification, and intercellular heterogeneity. (a) Optimal number of neighbors for UMAP embedding was determined using the *k*-nearest neighbor algorithm with the cosine distance metric where the optimal number of neighbors was determined to be $k = 4$. (b) UMAP two-dimensional plot of Cultured (blue) and UC Old (green) cell's pixels shows localized and relatively pure clusters with minimal overlap between the Cultured and UC Old cells. All MSI pixels belonging to each cell were included (i.e., multiple datapoints per cell). (c) UMAP two-dimensional plot showing Leiden assigned clusters where a total of 16 Leiden clusters were determined. (d) UMAP two-dimensional plot of all the MSI pixels acquired from each cell and colored by which cell it belongs to. Edges are visualized to show local connectivity between data points (gray lines). Localized Leiden clusters have pixels overlapping with other cell clusters within its own group and even between groups (i.e., Cultured, UC Old, and UC P1). Data points split between two different Leiden clusters of cells depict there is intracellular heterogeneity present within the same cell itself (i.e., cell body verses processes). (e) Feature significance from each classification task is then ranked using the minimum redundancy maximum relevance algorithm with the glycerophosphocholine lipid species *m/z* 734.5675 $(PC\ 32 + H)^+$ being ranked the most important for discrimination of Cultured vs UC Old cells. (f) Stacked violin plot visualizing the top 10 *m/z* features and their relative distribution in each group. The color scale represents the median mass spectral intensity in each group. (g, left) Merged brightfield and fluorescent images of immunostained cells for two cell-specific biomarkers: neuron—L1CAM+; astrocyte—GFAP+. The areas ablated by the laser microprobe shows the characteristic pattern imprinted during MS acquisition of the cells. (g, right) Subtracted mass spectra from each of the different cells with putatively identified lipid species annotated. The subtracted mass spectrum was created by normalizing each of the respective cell's mass spectrum and then subtracting the mass spectra from each other.

chemical complexity of lipids and the narrow mass range (mainly *m/z* 500–900) in which they are detected, making isobaric interference problematic for analyte identification.

In this work, we demonstrate the ability of a 21 T FTICR mass spectrometer to characterize the lipid profiles of isolated, individual rodent hippocampal cells. To explore how the lipid profiles of rodent hippocampal cells change due to cell culture conditions, we performed analysis on freshly isolated postnatal day one hippocampal cells (UC P1) and cultured primary hippocampal cells (Cultured) from the same animal, as well as freshly isolated cells from 2.0 to 2.5-month-old animals (UC Old) as an approximation of in vitro and in vivo conditions (Supplementary Figure 1). With numerous reports highlighting important differences in cell phenotype (including chemical profiles) and cell function between in vitro and in vivo conditions, characterizing the underlying chemical changes is

https://doi.org/10.1021/acs.analchem.3c00393
Anal. Chem. XXXX, XXX, XXX−XXX

important to understand the discrepancies between the two models.[21−24] This work demonstrates the utility of single-cell and subcellular 21 T FTICR MS for mapping the various chemical profiles that exist within the rodent hippocampus and how these profiles are altered due to different environmental conditions.

RESULTS AND DISCUSSION

21 T FTICR MS Single-Cell Analysis and Ultrahigh Mass Resolution for Isobaric Lipid Differentiation. Population of single-cells isolated from the rodent hippocampus was nuclear stained before plating on an indium tin oxide (ITO)-glass slide (Figure 1a,b), where brightfield and fluorescence microscopy were performed to find the relative locations of individual cells (Figure 1c). The UC P1 and UC Cultured cells were cultured on the ITO-glass slide and used poly-L-lysine for cell adherence, whereas the UC Old cells were not cultured on the ITO-slides but were isolated and glycerol added as a stabilizer while cells physically adhered to the ITO-glass slide. To probe the individual cells, a MS imaging (MSI) approach was taken to sample a large region of interest that encompassed the cells using a 30 μm raster step size (Figure 1d, top). After MSI analysis, an additional image of the ITO-glass slide was taken using brightfield microscopy and this image was overlayed onto the original microscopy image for visualization of the colocalization of both the ablated matrix positions and the corresponding single cells (Figure 1d, bottom). The location of each MALDI MS acquisition can then be visualized, and the corresponding mass spectrum discerned from the instrument's positional file. Using this approach, a total of eight Cultured cells, five UC Old cells, and six UC P1 cells were measured. Cell culture conditions have been shown to change the lipid metabolism of the cell, in turn altering cell composition and cell morphology.[25,26,26−28] The chemical complexity of lipids and the narrow mass range (mainly m/z 500−900) in which they are commonly detected in, make isobaric interference problematic in single-cell analysis. The issue is the inability to perform additional separation steps and/or tandem-MS analysis that allows differentiation of compounds that have similar masses. One of solution for this problem is increasing the resolving power of MS measurements. Here, a 21 T FTICR MS instrument achieved over a fivefold improvement in resolving power when compared to a 7 T instrument using the same transient acquisition time (Supplementary Figure 2). This improvement in mass resolution revealed the presence of $(PC\ 34{:}1 + H)^+$ and an additional overlapping isobaric peak, $(PC\ 34{:}2\ [M + 2] + H)^+$, where $(PC\ 34{:}2\ [M + 2] + H)^+$ represents the n + 2 isotope of $(PC\ 34{:}2 + H)^+$ (Figure 1e). Further increasing the transient acquisition time to 3.1 s gave a resolving power of over 1,000,000 at m/z 760.5850, making $(PC\ 34{:}2\ [M + 2] + H)^+$ fully resolvable from $(PC\ 34{:}1 + H)^+$ (Figure 1e, right). Additionally, an unidentified peak at m/z 760.58127 also appears between the two isobars when using a 3.1 s transient length. The unidentified peak and $(PC\ 34{:}1 + H)^+$ have a measured m/z of 760.58127 and 760.58506, respectively, making the mass difference 3.79 mDa. Comparing the average peaks detected per pixel in an entire MSI scan area shows the 3.1 s transient detecting 695 peaks whereas the 1.5 s transient detected 322, highlighting the isobaric problem.

Comparative Analysis of Lipid Profiles Detected in the Three Groups of Cells. To evaluate cell culture-induced lipid profile changes, an m/z range of 490−1075 was examined and as expected, two of the most abundant types of lipids found in each cell, across all cells were glycerophosphocholine lipids (e.g., m/z 734.5686 and m/z 760.5851) (Figure 1f). Glycerophosphocholine lipids are enriched in neuronal cells serving not only as structural components but also play roles in the regulation of cellular processes including the formation of microdomains in the plasma membrane.[29] With the UC P1 cells being on average at least two times smaller than the UC Old and Cultured cells, we aimed to find a reduced set of m/z features for the classification between the UC Old and Cultured cells (Figure 1g). Therefore, the top 100 significant m/z features for classification between UC Old and Cultured cells were identified using a two-sample t-test. To validate that the reduced number of lipid features can still adequately classify between the cell groups, linear discriminant analysis was performed for the Cultured UC P1 and UC Old cells, resulting in an overall classification accuracy of 97.1% (Figure 1h). It can be difficult to ascertain if MS data are normally distributed and that a nonparametric test may be more appropriate to use. To test this, we performed nonparametric Wilcoxon rank-sum test where it selected 75 of the same mass spectral features as the t-test and resulted in a near identical classification score. Therefore, without significant differences in the classification score, the t-test results are presented here. Running the top 100 significant m/z features against a lipid database resulted in the mass-match assignment of 18 putatively identified lipid species where use of a 21 T FTICR MS gave a 202 ppb root-mean-square mass accuracy for the detected lipids (Supplementary Table 1). Initially, 32 lipid species were identified by mass-match assignment within a 1 ppm mass tolerance, but without tandem-MS data, the lipids were curated to be consistent with what is observed in the literature and to remove an unusual lipid species. For example, odd chain saturated fatty acid lipid species and lipids not typically detected in positive mode were not included.

Lipid profile differences including stochastic heterogeneity can be expected between the three groups of cells (i.e., Cultured, UC P1, or UC Old), as well as both intercellularly and intracellularly.[30,31] To explore all three possibilities, a k-nearest neighbor classifier was used to determine optimal number of neighbors (Figure 2a) and the number of principal components were determined by plotting the variance ratio of the first 50 principal components (Supplementary Figure 3). Uniform manifold approximation and projection (UMAP) was performed to visualize the MSI pixels that belong to each cell and is color coded by group where clear separation can be seen between the UC Old and Cultured cells (Figure 2b). The lack of separation of the UC P1 cells may be attributed to their small size (<20 μm), which would give minimal signal intensity. With UMAP showing dense clustering of the different cell populations and 19 cells measured in total, we aimed to see if the MSI pixels belonging to each cell would form its own community. Therefore, Leiden clustering was performed which resulted in 16 detected Leiden clusters (Figure 2c).[32] Examination of the individual cell-related pixels shows pixels of each cell being split between different Leiden clusters, indicating that chemical differences can be detected both within and between cells (Figure 2d). Because cells were sampled multiple times, the split in pixels may correlate with different regions of the cell being measured (i.e., cell soma or cell processes).

The feature importance (Figure 2e) and feature distribution in each group was then visualized (Figure 2f). Looking at the

https://doi.org/10.1021/acs.analchem.3c00393
Anal. Chem. XXXX, XXX, XXX−XXX

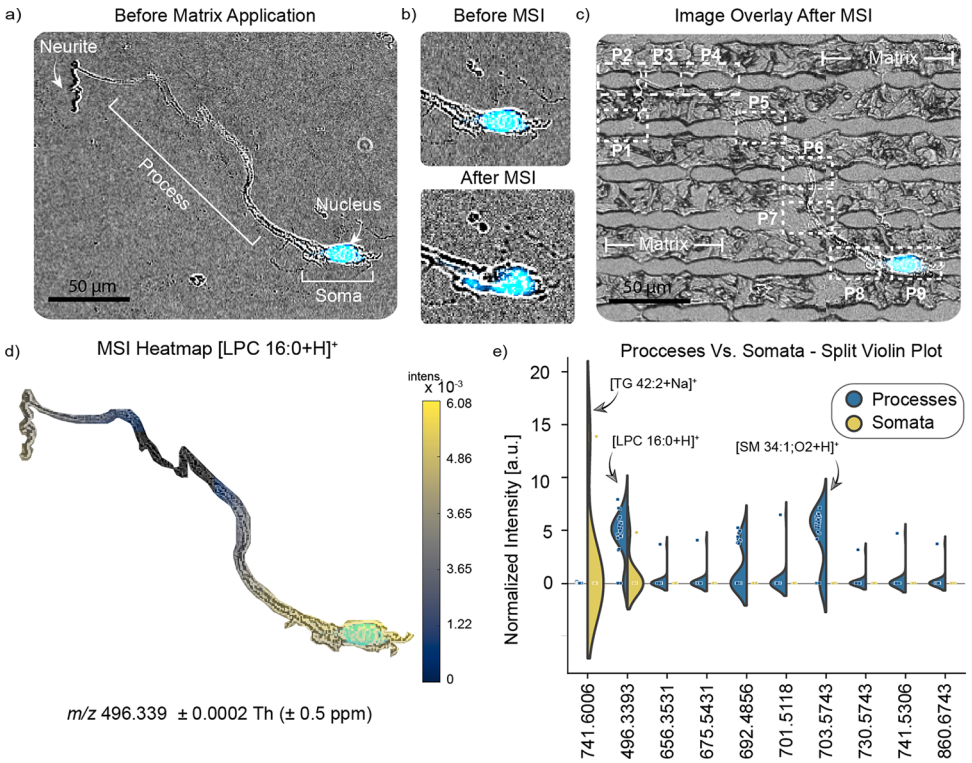

Figure 3. Subcellular 21 T FTICR MS analysis. (a) Merged brightfield and fluorescent image of a ∼250 μm long isolated single-cell (UC Old) before MALDI matrix application. (b) Comparison of cellular morphology before (top panel) and after (bottom panel) MALDI MS analysis. The before MSI photo shows the intact nucleus (blue) of the single-cell before MALDI MSI sampling. The after MS photo shows the same cell body and nucleus exposed to the laser beam and MALDI matrix. (c) Optical microscopy image after MSI analysis with the MALDI matrix still on the slide shows the spatial location of each individual laser-assisted data acquisition. The dashed white boxes represent each MALDI MS data acquisition where P1 denotes pixel one. (d) MSI heatmap showing the intensity distribution of LPC 16:0 $[M + H]^+$ across the length of single-cell. (e) Split violin plot showing the chemical differences between processes and cell somata for three measured single cells. Lipid species TG 42:2, LPC 16:0, and SM 34:1;O2 are annotated.

Cultured versus the UC Old cells, the Cultured cells show an increase in the sphingomyelin lipid, SM 34:1;O2 (m/z 703.5748-SM 34:1;O2), while the UC Old cells show the relative increase in glycerophospholipids, phosphatidylcholine (PC) 32:0 and PC 34:0. Glycerophospholipids are the most abundant lipid in mammalian plasma membranes, and with the Cultured and UC Old cells being approximately the same size, it interesting to see such a lower signal intensity for glycerophospholipids in the Cultured cells.[33] Comparing the average PC/SM ion intensity ratios in each cell shows a stark difference in the PC/SM ratio where the cultured cells have a ∼33:1 PC:SM ratio whereas the Cultured cells have a ∼1:3 PC:SM ratio (Supplementary Figure 5). Previous studies have demonstrated that the phosphocholine headgroup of PC is preferentially donated for SM synthesis and that different neuronal development stages have increases in SM during neuronal maturation, which may be why the unusual PC:SM ratio is observed in the Cultured cells.[34−36] Phosphatidylcholine and other choline containing compounds are major structural constituents of cell membrane, and the lipid composition at particular membrane locations is responsible for different physicochemical and morphological cellular parameters, including membrane curvature and fluidity. Even minor changes to PC ratios may lead to neuronal cell damage and even cell loss.[37] Phospholipid metabolism is central to the overall health of a cell where phospholipid metabolism has been shown to coordinate energy metabolism and aberrant PC metabolism has been associated with a pathophysiological state.[38]

Cell Typing Using Immunohistochemistry and Single-Cell 21 T FTICR MS Analysis. In neurobiology, cell type can be based on cellular morphology while single-cell MALDI MS provides details on the molecular content. Chemical information often lacks a structural and functional context, thus limiting the biological interpretations that can be drawn from MS measurements alone.[39−41] Coupled with the morphological diversity of neuronal cells, this makes correlating mass spectral profiles to conventional cell types challenging unless cell type specific markers are employed. To explore the subtle differences in cell lipid composition in relation to cell type, we employed immunocytochemical staining after MALDI MS analysis to classify cells. Immunocytochemistry after MALDI MS correlates the chemical detail with the canonical cell types found in the rodent hippocampus. Using this approach, we stained the single cells using primary antibodies against L1CAM, a neuronal marker and glial fibrillary acidic protein (GFAP), an astrocytic marker (Figure 2f, left). Thus, these stains allow us to categorize the cells as astrocytes, neurons, or others (cells that stained for neither marker). Using the correlated spatial locations of the single-cell and the laser-induced MALDI matrix ablation point, the mass spectrum produced by each labeled cell are subtracted from each other (Figure 2f, right). Although the overall lipid composition of the brain is relatively uniform, we observed the characteristic enrichment of

https://doi.org/10.1021/acs.analchem.3c00393
Anal. Chem. XXXX, XXX, XXX−XXX

sphingomyelin in the astrocyte when compared to neuronal cell where it is virtually absent.[39] The neuronal cell showed the enrichment in phosphatidylcholine and lysophosphatidylcholine (LPC), where LPC is expected to increase during neuronal differentiation.[39,42,43]

Subcellular 21 T FTICR MS Analysis. A laser microprobe that has a ∼25 μm footprint allows us to probe the soma and along a cellular process at multiple locations; this allows us to examine the chemical subcellular heterogeneity (Figure 3a−c). We performed optical microscopy of the ITO-glass slide after MALDI MS analyses with the MALDI matrix still on it. The images clearly show the sampling locations of the laser microprobe, such as along the length of a cellular process. Each MALDI MS acquisition is marked by the white boxes where P1 represents pixel one (Figure 3c). Using the mass spectral analyte peak intensity information from the different pixels, we create a heatmap and overlay it onto the single-cell using the single-cell as a clipping mask. While the use of the clipping mask can improve analyte visualization across the cell, it does not allow visualization of analyte delocalization. However, our observed chemical heterogeneity of cells located close to one another indicates that analyte delocalization does not play a significant role in the outcome of our measurements. Analyte delocalization can occur due to sample preparation, matrix application, or a cell's boundary being split between pixels. Figure 3d shows the intensity distribution of putative LPC 16:0 signal along the length of the cell. LPC is mainly derived from the turnover of PC by phospholipase A2.[44] Phospholipase A2 and other phospholipases have been shown to have expression in the nuclei of the cells and are responsible for the production of cell mediators and other bioactive signaling molecules.[45] Furthermore, secretory phospholipase A2 and LPC also exhibit neurotrophic like neuritogenic activity, which correlates with our observation of lysoposphatidylcholine signal in the neurite as well as the nucleus-containing cell body.[45]

Two additional cell results are shown showing chemical differences between cell bodies and cell processes (Supplementary Figure 6). Logistic regression was performed, and the top 400 significant m/z features were mass-matched to a lipid database. The split violin plot shows the normalized intensity distribution of putatively identified lipid species that were deemed important for differentiation between the nucleus-containing cell bodies (cell somata) and cell processes (Figure 3e). Interestingly, even with more sample material generally being present in the nucleus-containing cell bodies, only one m/z feature (TG 42:2) was found to be present solely in the cell bodies. Immunogold electron microscopy showed localization of triacylglycerol hydrolase in the endoplasmic reticulum, specifically in regions surrounding the mitochondria which aligns with our results.[46] Besides LPC 16:0, the remaining lipid features were found only in the processes of the cells measured. Sphingomyelin synthase's (SMS) two isoforms, sphingomyelin synthases 1 (SMS1) and sphingomyelin synthase 2 (SMS2), have been shown to be expressed in different cellular locations depending on the neuronal subtype. In SM1-expressing neurons, sphingomyelin clusters were present in the cell body but not processes, whereas in SM2-expressing neurons, sphingomyelin clusters were present in the processes, which supports our observation of analyte signal of SM 34:1;O2 in the processes but not nucleus-containing cell bodies.[47]

CONCLUSIONS

Here, we demonstrated single-cell and subcellular analysis using the ultrahigh mass resolution of a MALDI 21 T FTICR mass spectrometer which represents a significant advance in the bioanalytical capabilities that allowed higher analyte coverage and confidence in analyte identification. This work expands our previous work by serving as a comparison of lipid profile differences between in vitro and in vivo conditions, where previous work focused on in vivo conditions using whole-cell profiling with a ∼100 μm laser spot size. The work expands upon the analysis by increasing mass accuracy and resolution allowing the differentiation of isobaric lipid species with a 3.79 mDa mass difference. Finally, utilization of a laser microprobe with a footprint smaller (∼25 μm) than the cells themselves allowed the exploration and comparative analysis of both subcellular and intercellular heterogeneity.

METHODS

General. All chemicals were obtained from Sigma-Aldrich unless specified otherwise.

Animals. Male Sprague−Dawley outbred rats (*Rattus norvegicus*) were obtained from Envigo (https://www.envigo.com/), fed ad libitum, and housed on a 12 h light cycle. Long-Evans, genetically homogeneous, BluGill rat line were bred and maintained by the Gillette lab.[48,49] Animal euthanasia was performed in accordance with the Illinois Institutional Animal Care and Use Committee and both federal and ARRIVE guidelines for the humane care and treatment of animals.

Single-Cell Dissociation of 2.0 to 2.5-Month-Old Male Rats. A total of three 2.0 to 2.5-month-old male Sprague−Dawley rats were used for single hippocampal cell isolation (marked as UC Old cells). Each isolated tissue region was individually treated with a papain dissociation system (Worthington Biochemical, Lakewood, NJ) and incubated for 120 min at 34 °C with oxygenation. The treated tissue regions were then mechanically dissociated in modified Gey's balanced salt solution (mGBSS) containing: 1.5 mM $CaCl_2$, 5 mM KCl, 0.2 mM KH_2PO_4, 11 mM $MgCl_2$, 0.3 mM $MgSO_4$, 138 mM NaCl, 28 mM $NaHCO_3$, 0.8 mM Na_2HPO_4, and 25 mM HEPES, pH 7.2 and supplemented with 0.08% paraformaldehyde to stabilize cells against damage during dissociation. A solution of 80% glycerol and 20% mGBSS was added to each vial containing tissue dissociates to a final glycerol concentration of 40% (v/v), and the cells were stained with Hoechst 33342 (0.1 μg/mL in mGBSS) before an aliquot of cell suspension was plated onto an ITO-coated unpolished float glass slide, R_s = 70−100 Ω (Delta Technologies, Loveland, CO) before rinsing with 150 mM ammonium acetate.

Single-Cell Dissociation and Culture of P1 Cells. Hippocampal cells were isolated from a postnatal day one (P1) Long-Evans, genetically homogeneous, BluGill rat. Cells were maintained in Hibernate-A (Brain-Bits, Springfield, IL) media supplemented with 2% B-27 Plus (Invitrogen Waltham, MA), 1% 100 U/mL penicillin, 0.1 mg/mL streptomycin, and 0.25% GlutaMAX (Invitrogen). Once isolated, the hippocampus was digested with papain (18.75 U/mL) for 30 min at 37 °C. The hippocampus was further broken down by gentle trituration using a fire polished glass Pasteur pipette, then strained through a 40 μm cell filter (Corning Glendale, AZ), and finally suspended in Neurobasal-A (Invitrogen) media which supplemented the same as Hibernate-A media. Once isolated,

https://doi.org/10.1021/acs.analchem.3c00393
Anal. Chem. XXXX, XXX, XXX−XXX

the hippocampal neurons were maintained at 37 °C and 5% CO_2. ITO-glass slides were coated with 0.1 mg/mL poly-L-lysine before rinsing with deionized water. P1 cells were counted in a hemacytometer and contained ∼2 million cells per milliliter. A 50 μL aliquot was plated on the ITO-slide and allowed to adhere in a Petri dish for 1 h at 37 °C in 5% CO_2 and ambient oxygen. Afterward, the Petri dish was flooded with approximately 20 mL of media and allowed to incubate for 4 days. The cells were then stained by addition of Hoechst 33342 to the media for a final concentration of 0.1 μg/mL and allowed to incubate for 9 min. The media was then aspirated, and the slide was washed with phosphate buffered solution (PBS) three times followed by three 150 mM ammonium acetate rinses.

Single-Cell Immunocytochemistry. After MSI analysis, the MALDI matrix was removed during the fixation process by sample incubation with 4% paraformaldehyde in PBS for 9 min. The cells were then washed with PBS three times before blocking for 1 h at room temperature in a blocking solution consisting of 1 mg/mL BSA, 10% (v/v) goat serum, and 0.1% Tween-20 in PBS. The blocking buffer was removed by three washes using PBS, and the cells were stained with primary antibodies against L1CAM (ab24345) and GFAP (ab7260) (Abcam, Cambridge, U.K.), both at a concentration of 1:1000 for 2 days at 4 °C. Primary antibodies were removed by three washes of PBS and stained with goat anti-mouse Alexa Fluor 594 (ab150120) and Alexa Fluor 488 (ab150081) secondary antibodies at a concentration of 2.5:1000 for 2 h at room temperature. The secondary antibody solution was removed before optical imaging of the sample by three washes of PBS.

Brightfield and Fluorescence Microscopy. Brightfield and fluorescent images were acquired on an Axio Imager M2 (Zeiss, Jena, Germany) equipped with an AxioCam ICc 5 using a .63× camera adaptor, transmitted light VIS-LED lamp, and X-cite Series 120 Q mercury lamp (Lumen Dynamics, Mississauga, Canada). DAPi (ex. 335−383 nm; em. 420−470 nm), GFP (ex. 450−490 nm; em. 500−550), and HE DsRed (ex. 538−562; em. 570−640) dichroic filter cubes were used for imaging. Images were acquired in mosaic mode using a 10× objective with 10% tile overlap. The resulting tiles were stitched before exporting in TIFF-file format using ZEN 2.0 Pro edition (Zeiss, Jena, Germany) software. Unstained controls were acquired for linear unmixing.

MALDI Matrix Application. The MALDI matrix 2,5-dihydroxybenzoic acid (DHB) was prepared to a concentration of 75 mg/mL in 70% methanol. Matrix was applied using a HTX-M5 Sprayer (HTX Technologies, Chapel Hill, NC) with a spray spacing of 2.5 mm at a nozzle temperature of 75 °C using a flow rate of 100 μL/min. The distance of the sprayer nozzle from the sample was 50 mm, and a spray pressure of 10 psi with a spray velocity of 1200 mm/min was used. The sample was sprayed using one pass of the HTX-M5 sprayer.

Single-Cell Pixel Selection and Image Overlay. For finding and selection of pixels corresponding to single cells and subcellular structures, an image overlay was performed in MATLAB 2020b (MathWorks) and ZEN 2.0 Pro edition (Zeiss) software. Single-cell images were acquired after MALDI MS analysis with the MALDI matrix still covering the slide using ZEN 2.0 Pro edition software. The original (before MALDI matrix application) and after MALDI MS analysis sample images were overlaid using ZEN 2.0 Pro edition software's overlay function using etched on the ITO-coated glass slide fiducial markers for alignment. The pixel size and MALDI laser footprint diameter and height were also determined. Using the ablated matrix spots as a guide, the individual areas (regions of interest) on the images were cropped and exported in TIFF-file format. The cropped images and raw MS data were then loaded into a MATLAB application, MSiReader.[50] Using the microscopy images to determine the dimensions ablated by laser microprobe, the pixels were scaled accordingly and the number of pixels were determined from the extensible markup language (XML) instrument position file. The cropped image was then overlayed onto the previously overlaid, before and after MALDI MSI single-cell images. Selection of single-cell pixels was done using MSiReader's pixel selection tool, and mass spectrometric scan information from the region of interest was exported. The scan numbers were then used to parse the corresponding mass spectra from the entire data set.

Data Preprocessing and Analysis. Magnitude mode mass spectra were used for analysis. Data preprocessing was performed using MATLAB 2020b (MathWorks) and Python-based open source packages, SCANPY[51] and Scikit-learn.[52] The single-cell and subcellular mass spectra were aligned over the m/z range of 490−1075 using a uniform bin width of 0.01 Da.[53] The aligned data matrix was then passed to Python open-source package SCANPY for total ion count (TIC) normalization. The optimal number of neighbors was determined using Scikit's KNeighborsClassifier, and the number of principal components for UMAP embedding was determined in SCANPY by inspecting the contribution of the top 50 principal components to the total variance in the data set. Next two sample t-test was performed to identify significant m/z features between the Cultured and UC Old cells. The top 100 features were then matched to a lipid database[51] using a mass tolerance of less than 0.005 Da. The 100 m/z features were then passed to MATLAB 2020b for classification between the three groups using linear regression. Mass accuracy of MS measurements was calculated from the unaligned raw data due to the use of a large bin width of 0.01 Da to prevent peak splitting. For differentiation between nucleus-containing cell bodies and cell processes, the m/z range of 450−1075 was aligned using a uniform bin width of 0.01 Da. Logistic regression was performed to identify significant m/z features, and the top 400 features were matched to a lipid database.[10]

7 T MALDI MS Measurements. Single-cell measurements as a comparison to the 21 T FTICR mass spectrometer were performed on a 7 T FTICR mass spectrometer (Bruker Corp., Billerica, MA) equipped with an APOLLO II dual MALDI/ESI source (Bruker). Data were collected at 1 M yielding a transient acquisition time of 0.721 s for m/z range 150−1600 and 0.979 s for m/z range 200−1600, respectively. Data were also collected at 2 M for m/z range 200−1600 yielding a transient acquisition time of 1.478 s. The instrument was operated in positive-mode using a Smartbeam-II UV laser (Bruker) set to "ultra mode," which yields a 100 μm-diameter laser footprint. Each MALDI acquisition consisted of one accumulation comprising of 400 laser shots each, at a frequency of 1000 Hz. Single-cell stage coordinates were generated using microMS as previously described.[14]

21 T MALDI MSI Measurements. Ultrahigh mass resolution single-cell MALDI imaging experiments were carried out on the 21 T FTICR instrument at the National High Magnetic Field Laboratory (NHMFL). The hybrid system is a modified dual linear ion trap (Velos Pro) coupled

https://doi.org/10.1021/acs.analchem.3c00393
Anal. Chem. XXXX, XXX, XXX−XXX

to a dynamically harmonized ICR cell, designed and built by NHMFL, operated with a 21 T Bruker superconducting magnet.[54] The ICR cell is operated at a 7.5 V trapping potential, and 1.5 and 3.1 s transients were acquired.

For MALDI MS imaging experiments, an elevated-pressure MALDI ion source with a dual ion funnel interface was used (Spectroglyph LLC, Kennewick, WA, USA).[55] Radiofrequency voltages within the funnels were 741 kHz, 180 V_{p-p} in the high-pressure funnel and 873 kHz, 80 V_{p-p} in the low-pressure funnel. An electric field gradient of ~90 V cm^{-1} between the sample plate and funnel inlet was applied. The system uses a Q-switched frequency-tripled Nd:YLF laser emitting 349 nm light (Explorer One, Spectra Physics, Mountain View, CA). The laser was operated at a repetition rate of 400 Hz and a pulse energy of ~1 μJ. Pressure within the source was set to 7.3 Torr in the ion funnel and MALDI stage. Automatic gain control was turned off on the system with a set injection time of 500 ms. An area of interest was measured with the MALDI laser using a 30 μm step size in both directions. The approximate laser dimensions of the microprobe footprint were 25 × 15 μm.

■ ASSOCIATED CONTENT

Supporting Information

The Supporting Information is available free of charge at https://pubs.acs.org/doi/10.1021/acs.analchem.3c00393.

> Supplemental information is available for this paper and consists of a table of detected lipids, and the following figures: single-cell images of hippocampal cells, a comparison of the theoretical versus measured mass resolution, variance ratio and principal component analyses, the top 33 m/z features for each experimental cell group, a phosphatidylcholine and sphingomyelin comparison for different treatment groups, further examples of single-cell MSI, and the differential m/z features for differentiation between cell processes and cell soma (PDF)

Accession Codes

The code used in this study is publicly available on Github (https://github.com/dcast0075/Single-cell-and-Subcellular-Analysis-using-Ultrahigh-Resolution-21-T-MALDI-FTICR-Mass-Spectrometry).

■ AUTHOR INFORMATION

Corresponding Author

Jonathan V. Sweedler − *Department of Molecular and Integrative Physiology, University of Illinois at Urbana-Champaign, Urbana, Illinois 61801, United States; Department of Chemistry, University of Illinois at Urbana-Champaign, Urbana, Illinois 61801, United States; Neuroscience Program and Beckman Institute for Advanced Science and Technology, University of Illinois at Urbana-Champaign, Urbana, Illinois 61801, United States; Department of Bioengineering, University of Illinois at Urbana-Champaign, Urbana, Illinois 61801, United States;* orcid.org/0000-0003-3107-9922; Email: jsweedle@illinois.edu

Authors

Daniel C. Castro − *Department of Molecular and Integrative Physiology, University of Illinois at Urbana-Champaign, Urbana, Illinois 61801, United States; Beckman Institute for Advanced Science and Technology, University of Illinois at Urbana-Champaign, Urbana, Illinois 61801, United States;* orcid.org/0000-0002-9127-6242

Karl W. Smith − *National High Magnetic Field Laboratory, Florida State University, Tallahassee, Florida 32310, United States;* Present Address: Leibniz-Institut für Analytische Wissenschaften-ISAS-e.V., Otto-Hahn Straße 6b, 44139 Dortmund, Germany

Miles D. Norsworthy − *Beckman Institute for Advanced Science and Technology, University of Illinois at Urbana-Champaign, Urbana, Illinois 61801, United States; Department of Cell and Developmental Biology, University of Illinois at Urbana-Champaign, Urbana, Illinois 61801, United States*

Stanislav S. Rubakhin − *Department of Chemistry, University of Illinois at Urbana-Champaign, Urbana, Illinois 61801, United States; Neuroscience Program and Beckman Institute for Advanced Science and Technology, University of Illinois at Urbana-Champaign, Urbana, Illinois 61801, United States;* orcid.org/0000-0003-0437-1493

Chad R. Weisbrod − *National High Magnetic Field Laboratory, Florida State University, Tallahassee, Florida 32310, United States;* orcid.org/0000-0001-5324-4525

Christopher L. Hendrickson − *National High Magnetic Field Laboratory, Florida State University, Tallahassee, Florida 32310, United States;* orcid.org/0000-0002-4272-2939

Complete contact information is available at: https://pubs.acs.org/10.1021/acs.analchem.3c00393

Author Contributions

J.V.S, C.L.H., and C.R.W. conceived the project idea and provided direction throughout. S.S.R. and M.D.N. performed the single-cell dissociations. D.C.C. prepared and cultured samples for MALDI MSI, performed ICC labeling, acquired microscopy images, and performed data analysis. K.W.S. developed the MS method and acquired 21 T data. C.L.H and C.R.W. provided feedback and guidance on 21 T method development and data acquisition. D.C.C. created the figures and wrote the manuscript which was edited by all authors. We thank the Gillette lab for providing cells when they were needed most.

Notes

The authors declare no competing financial interest.

The data that support the findings of this study are publicly available on the Illinois Data Bank (https://doi.org/10.13012/B2IDB-4873339_V1).

■ ACKNOWLEDGMENTS

This project was supported by the National Institute on Drug Abuse under Award no. P30DA018310, the National Human Genome Research Institute under Award no. R01HG010023, and the NSF National Research Traineeship on Miniature Brain Machinery NSF DGE 17-35252. The content is solely the responsibility of the authors and does not necessarily represent the official views of the awarding agencies. The ICR User Facility at the National High Magnetic Field Laboratory is supported by the National Science Foundation Division of Chemistry and Division of Materials Research through DMR-1644779, and the State of Florida.

■ REFERENCES

(1) Alves-Bezerra, M.; Cohen, D. E. *Compr. Physiol.* **2017**, *8*, 1−8.

(2) Nguyen, P.; Leray, V.; Diez, M.; Serisier, S.; Le Bloc'h, J.; Siliart, B.; Dumon, H. *J. Anim. Physiol. Anim. Nutr.* **2008**, *92*, 272−283.
(3) Clamp, A. G.; Ladha, S.; Clark, D. C.; Grimble, R. F.; Lund, E. K. *Lipids* **1997**, *32*, 179−184.
(4) Sunshine, H.; Iruela-Arispe, M. L. *Curr. Opin. Lipidol.* **2017**, *28*, 408−413.
(5) Fruhwirth, G. O.; Loidl, A.; Hermetter, A. *Biochim. Biophys. Acta, Mol. Basis Dis.* **2007**, *1772*, 718−736.
(6) Halliwell, B. *FEBS Lett.* **2003**, *540*, 3−6.
(7) Bhaduri, A.; Neumann, E. K.; Kriegstein, A. R.; Sweedler, J. V. *JACS Au* **2021**, *1*, 2261−2270.
(8) Angerer, T. B.; Magnusson, Y.; Landberg, G.; Fletcher, J. S. *Anal. Chem.* **2016**, *88*, 11946−11954.
(9) Spector, A. A.; Yorek, M. A. *J. Lipid Res.* **1985**, *26*, 1015−1035.
(10) Sud, M.; Fahy, E.; Cotter, D.; Brown, A.; Dennis, E. A.; Glass, C. K.; Merrill, A. H.; Murphy, R. C.; Raetz, C. R. H.; Russell, D. W.; Subramaniam, S. *Nucleic Acids Res.* **2007**, *35*, D527−D532.
(11) Yee, S. M.; Gillams, R. J.; McLain, S. E.; Lorenz, C. D. *Soft Matter* **2021**, *17*, 126−135.
(12) Han, X. *Nat. Rev. Endocrinol.* **2016**, *12*, 668−679.
(13) Yang, K.; Han, X. *Trends Biochem. Sci.* **2016**, *41*, 954−969.
(14) Comi, T. J.; Neumann, E. K.; Do, T. D.; Sweedler, J. V. *J. Am. Soc. Mass Spectrom.* **2017**, *28*, 1919−1928.
(15) Bien, T.; Bessler, S.; Dreisewerd, K.; Soltwisch, J. *Anal. Chem.* **2021**, *93*, 4513−4520.
(16) Niehaus, M.; Soltwisch, J.; Belov, M. E.; Dreisewerd, K. *Nat. Methods* **2019**, *16*, 925−931.
(17) Rappez, L.; Stadler, M.; Triana, S.; Gathungu, R. M.; Ovchinnikova, K.; Phapale, P.; Heikenwalder, M.; Alexandrov, T. *Nat. Methods* **2021**, *18*, 799−805.
(18) Bowman, A. P.; Blakney, G. T.; Hendrickson, C. L.; Ellis, S. R.; Heeren, R. M. A.; Smith, D. F. *Anal. Chem.* **2020**, *92*, 3133−3142.
(19) Smith, D. F.; Podgorski, D. C.; Rodgers, R. P.; Blakney, G. T.; Hendrickson, C. L. *Anal. Chem.* **2018**, *90*, 2041−2047.
(20) Scigelova, M.; Hornshaw, M.; Giannakopulos, A.; Makarov, A. *Mol. Cell. Proteomics* **2011**, *10*, No. M111.009431.
(21) Ackermann, T.; Tardito, S. *Trends Cancer* **2019**, *5*, 329−332.
(22) Biancur, D. E.; Paulo, J. A.; Małachowska, B.; Quiles Del Rey, M.; Sousa, C. M.; Wang, X.; Sohn, A. S. W.; Chu, G. C.; Gygi, S. P.; Harper, J. W.; Fendler, W.; Mancias, J. D.; Kimmelman, A. C. *Nat. Commun.* **2017**, *8*, 15965.
(23) Davidson, S. M.; Papagiannakopoulos, T.; Olenchock, B. A.; Heyman, J. E.; Keibler, M. A.; Luengo, A.; Bauer, M. R.; Jha, A. K.; O'Brien, J. P.; Pierce, K. A.; Gui, D. Y.; Sullivan, L. B.; Wasylenko, T. M.; Subbaraj, L.; Chin, C. R.; Stephanopolous, G.; Mott, B. T.; Jacks, T.; Clish, C. B.; Vander Heiden, M. G. *Cell Metab.* **2016**, *23*, 517−528.
(24) Vande Voorde, J.; Ackermann, T.; Pfetzer, N.; Sumpton, D.; Mackay, G.; Kalna, G.; Nixon, C.; Blyth, K.; Gottlieb, E.; Tardito, S. *Sci. Adv.* **2019**, *5*, No. eaau7314.
(25) Ghioni, C.; Tocher, D. R.; Sargent, J. R. *Fish Physiol. Biochem.* **1997**, *16*, 499−513.
(26) Ouellette, M.-È.; Bérubé, J.-C.; Bourget, J.-M.; Vallée, M.; Bossé, Y.; Fradette, J. *PLoS One* **2019**, *14*, No. e0224228.
(27) Savonnière, S.; Zeghari, N.; Miccoli, L.; Muller, S.; Maugras, M.; Donner, M. *J. Biotechnol.* **1996**, *48*, 161−173.
(28) Yaqoob, P.; Newsholme, E. A.; Calder, P. C. *Biochim. Biophys. Acta, Lipids Lipid Metab.* **1995**, *1255*, 333−340.
(29) Bochkov, V. N.; Oskolkova, O. V.; Birukov, K. G.; Levonen, A.-L.; Binder, C. J.; Stöckl, J. *Antioxid. Redox Signaling* **2010**, *12*, 1009−1059.
(30) Fergusont, K. A. *Proc. Natl. Acad. Sci. U. S. A.* **1974**, *71*, 4072−4076.
(31) Kankaanpä, P.; Yang, B.; Kallio, H.; Isolauri, E.; Salminen, S. *Appl. Environ. Microbiol.* **2004**, *70*, 129−136.
(32) Traag, V. A.; Waltman, L.; van Eck, N. J. *Sci. Rep.* **2019**, *9*, 5233.
(33) Poitelon, Y.; Kopec, A. M.; Belin, S. *Cell* **2020**, *9*, 812.
(34) Trovò, L.; Van Veldhoven, P. P.; Martín, M. G.; Dotti, C. G. *J. Cell Sci.* **2011**, *124*, 1308−1315.
(35) Yeh, Y.-Y. *J. Neurosci. Res.* **1984**, *11*, 383−394.
(36) Prinetti, A.; Chigorno, V.; Prioni, S.; Loberto, N.; Marano, N.; Tettamanti, G.; Sonnino, S. *J. Biol. Chem.* **2001**, *276*, 21136−21145.
(37) Mulder, C.; Wahlund, L.-O.; Teerlink, T.; Blomberg, M.; Veerhuis, R.; van Kamp, G. J.; Scheltens, P.; Scheffer, P. G. *J. Neural Transm.* **2003**, *110*, 949−955.
(38) van der Veen, J. N.; Kennelly, J. P.; Wan, S.; Vance, J. E.; Vance, D. E.; Jacobs, R. L. *Biochim. Biophys. Acta, Biomembr.* **2017**, *1859*, 1558−1572.
(39) Fitzner, D.; Bader, J. M.; Penkert, H.; Bergner, C. G.; Su, M.; Weil, M.-T.; Surma, M. A.; Mann, M.; Klose, C.; Simons, M. *Cell Rep.* **2020**, *32*, No. 108132.
(40) Kriegstein, A. R.; Dichter, M. A. *J. Neurosci.* **1983**, *3*, 1634−1647.
(41) Laturnus, S.; Kobak, D.; Berens, P. *Neuroinformatics* **2020**, *18*, 591−609.
(42) Neumann, E. K.; Comi, T. J.; Rubakhin, S. S.; Sweedler, J. V. *Angew. Chem., Int. Ed.* **2019**, *58*, 5910−5914.
(43) Riebeling, C.; Futerman, A. H. *Ceramide in the Regulation of Neuronal Development: Two Faces of a Lipid*; Landes Bioscience, 2013.
(44) Lee, J. C.-M.; Simonyi, A.; Sun, A. Y.; Sun, G. Y. *J. Neurochem.* **2011**, *116*, 813−819.
(45) Joensuu, M.; Wallis, T. P.; Saber, S. H.; Meunier, F. A. *J. Neurochem.* **2020**, *153*, 300−333.
(46) Gilham, D.; Alam, M.; Gao, W.; Vance, D. E.; Lehner, R. *Mol. Biol. Cell* **2005**, *16*, 984−996.
(47) Kidani, Y.; Ohshima, K.; Sakai, H.; Kohno, T.; Baba, A.; Hattori, M. *Biochem. Biophys. Res. Commun.* **2012**, *417*, 1014−1017.
(48) Millet, L. J.; Stewart, M. E.; Sweedler, J. V.; Nuzzo, R. G.; Gillette, M. U. *Lab Chip* **2007**, *7*, 987−994.
(49) Millet, L. J.; Stewart, M. E.; Nuzzo, R. G.; Gillette, M. U. *Lab Chip* **2010**, *10*, 1525−1535.
(50) Robichaud, G.; Garrard, K. P.; Barry, J. A.; Muddiman, D. C. *J. Am. Soc. Mass Spectrom.* **2013**, *24*, 718−721.
(51) Wolf, F. A.; Angerer, P.; Theis, F. J. *Genome Biol.* **2018**, *19*, 15.
(52) Pedregosa, F.; Varoquaux, G.; Gramfort, A.; Michel, V.; Thirion, B.; Grisel, O.; Blondel, M.; Prettenhofer, P.; Weiss, R.; Dubourg, V.; Vanderplas, J.; Passos, A.; Cournapeau, D.; Brucher, M.; Perrot, M.; Duchesnay, É. *J. Mach. Learn. Res.* **2011**, *12*, 2825−2830.
(53) Sud, M.; Fahy, E.; Cotter, D.; Azam, K.; Vadivelu, I.; Burant, C.; Edison, A.; Fiehn, O.; Higashi, R.; Nair, K. S.; Sumner, S.; Subramaniam, S. *Nucleic Acids Res.* **2016**, *44*, D463−D470.
(54) Hendrickson, C. L.; Quinn, J. P.; Kaiser, N. K.; Smith, D. F.; Blakney, G. T.; Chen, T.; Marshall, A. G.; Weisbrod, C. R.; Beu, S. C. *J. Am. Soc. Mass Spectrom.* **2015**, *26*, 1626−1632.
(55) Belov, M. E.; Ellis, S. R.; Dilillo, M.; Paine, M. R. L.; Danielson, W. F.; Anderson, G. A.; de Graaf, E. L.; Eijkel, G. B.; Heeren, R. M. A.; McDonnell, L. A. *Anal. Chem.* **2017**, *89*, 7493−7501.

https://doi.org/10.1021/acs.analchem.3c00393
Anal. Chem. XXXX, XXX, XXX−XXX